One-step Noisy Label Mitigation

Hao Li[1*]
18th.leolee@gmail.com

Jiayang Gu[1*]
jiayang.barrygu@gmail.com

Jingkuan Song[1†]
jingkuan.song@gmail.com

An Zhang[2]
anzhang@u.nus.edu

Lianli Gao[1]
lianli.gao@uestc.edu.cn

[1]University of Electronic Science and Technology of China
[2]National University of Singapore

Abstract

Mitigating the detrimental effects of noisy labels on the training process has become increasingly critical, as obtaining entirely clean or human-annotated samples for large-scale pre-training tasks is often impractical. Nonetheless, existing noise mitigation methods often encounter limitations in practical applications due to their task-specific design, model dependency, and significant computational overhead. In this work, we exploit the properties of high-dimensional orthogonality to identify a robust and effective boundary in cone space for separating clean and noisy samples. Building on this, we propose One-step Anti-Noise (OSA), a model-agnostic noisy label mitigation paradigm that employs an estimator model and a scoring function to assess the noise level of input pairs through just one-step inference, a cost-efficient process. We empirically demonstrate the superiority of OSA, highlighting its enhanced training robustness, improved task transferability, ease of deployment, and reduced computational costs across various benchmarks, models, and tasks. Our code is released at https://github.com/leolee99/OSA.

1 Introduction

Noise mitigation aims to handle the detriment of noisy labels encountered during the training process. The advancement of large-scale pre-training has significantly increased data scale to the trillion level. Much of this data is sourced from the internet, inevitably introducing considerable noise, which severely impedes the training process. This poses a substantial challenge for robust model training in various tasks, such as cross-modal matching [1, 2], image-classification [3, 4], and image-retrieval [5].

Traditional noise mitigation approaches encounter several limitations that constrain their practical applicability: 1) **Task specificity:** Existing methods [1, 3, 6] are tailored to specific tasks, limiting their applicability across different tasks. 2) **Model dependency:** Most noise mitigation techniques [5, 7] are tightly coupled with specific models, requiring extensive modifications for adaptation to different models. 3) **Computational cost:** Numerous existing methods necessitate dual-model collaborations [1, 4] or multiple training passes [1], *i.e.*, they require at least two backward passes per training step, effectively doubling the computational expense and substantially increasing the training burden (see Figure. 1a).

To tackle these challenges, we use an external estimator to assess the noise level of each sample, ensuring a model-agnostic approach. This estimator adjusts the training loss by reducing the influence

---

[*]Equal Contribution.

[†]Corresponding author.

Preprint. Under review.

| | Warm up | Clarify data | Rectify data | Co-training |

(a) Multiple backwards enhancing cost

(b) Task paradigm unification

(c) CLIP on COCO

(d) ALIGN on COCO

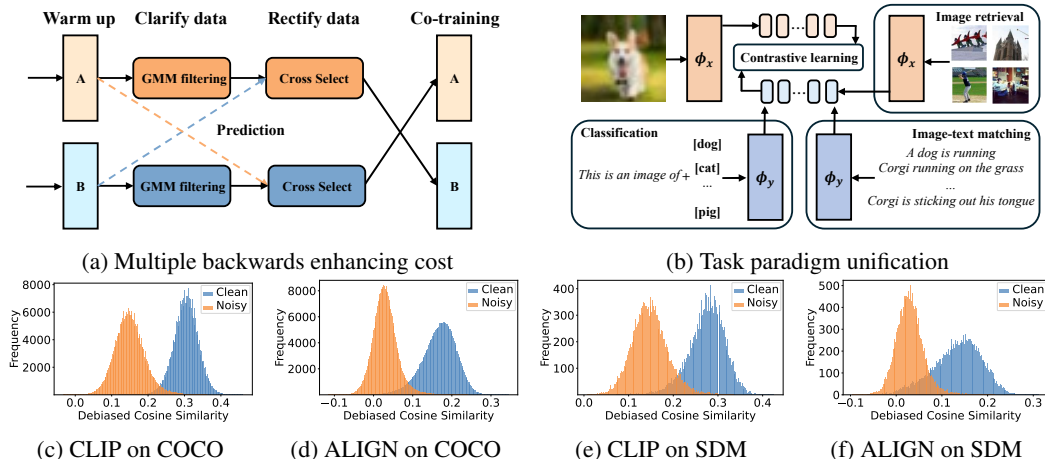(e) CLIP on SDM

(f) ALIGN on SDM

Figure 1: **(a)** The current anti-noise paradigm with multiple backward significantly enhances the training overhead. **(b)** CLIP unifies the framework of image-text matching and image classification through a shared space. **(c-f)** Cosine similarity distribution of noise and clean data with 50% noise.

of noisy samples, driving their weights toward zero. Furthermore, multimodal pre-trained models have demonstrated remarkable task transferability due to their strong semantic capabilities. For instance, CLIP [8] unifies the paradigms of image-text retrieval and image classification through a shared embedding space (see Figure. 1b). It converts category labels into sentences, maps them into the shared embedding space, and then calculates the cosine similarity with the image representation to perform image classification. Inspired by this, we leverage multimodal pre-trained models as estimators and apply the shared embedding space to enable task transfer. In this case, only one additional inference process is required for each sample, significantly reducing the computational overhead compared to performing an extra backward pass.

Nonetheless, this paradigm introduces a new challenge: how to accurately identify noise based solely on cosine similarity scores generated by estimators. An ideal solution is to find a decision boundary that separates clean samples from noise and accurately handles overlapping samples near the boundary. Existing methods [1, 9, 10, 2] typically attempt to build this boundary within the loss space, an isotropic space with uniform distribution, which creates only a narrow gap between noisy and clean samples. Moreover, the coarse handling of overlaps by integrating multi-model predictions often results in an unstable decision boundary. In contrast, the shared embedding space of pre-trained models is a high-dimensional, anisotropic space with an imbalanced distribution. Thus, a consideration is whether the properties of imbalanced anisotropic space can help to identify a more precise and robust decision boundary.

In this work, we delve into the decision boundary of pre-trained models employed as estimators to accurately differentiate between clean and noisy samples. We first investigate the cosine similarity distributions of clean and noisy samples, calculated using the multimodal pre-trained models CLIP [8] and ALIGN [11], on two datasets with a 50% noise ratio: MS-COCO [12] and SDM, as shown in Figure. 1c-1f. SDM is a dataset with the images generated by the Stable Diffusion Model (SDM) [13] in some uncommon styles (see illustrations in Figure. 4). It is designed to explore how well pre-trained models can distinguish unfamiliar domains that they rarely encounter during training. There are two interesting observations in Figure. 1c-1f: **(1)** The clean and noisy distributions of the same model on different datasets have a similar intersection point, suggesting the existence of a natural and stable boundary in distinguishing between clean and noisy samples. **(2)** The overlaps between the clean distribution and noisy distribution are minimal even in the unfamiliar domain dataset, indicating this boundary has strong potential for distinguishing between clean and noisy samples.

Building upon these two observations, we conduct an in-depth investigation and make the following contributions:

1. We figure out the origin of the intersection, attributing it to the shift in the orthogonal boundary induced by the cone effect. Furthermore, we provide a theoretical framework that proves and elaborates the stability and precision of this boundary in separating noisy and clean samples.

2. We provide a detailed explanation of the reliability of pre-trained models in general noise recognition, even in unfamiliar domains, grounded in the analysis of the pre-training process.

3. Build on this, we introduce One-Step Anti-Noise (OSA), a general model-agnostic paradigm for noise recognition that requires only one-step inference. Specifically, we utilize a pre-trained model as the estimator to maintain a shared embedding space. A scoring function, designed based on the properties of high-dimensional orthogonality, is then used to accurately handle overlaps by directly assigning a learning weight to each sample's loss according to its cosine similarity.

4. We conduct comprehensive experiments across a variety of challenging benchmarks, models, and tasks, demonstrating the effectiveness, generalization capabilities, and efficiency of our method.

2 Boundary Principle Analysis

In Figure. 1c-1f, we observe a natural boundary emerging in the pre-trained model's ability to distinguish between clean and noisy samples. In this section, we explain the principle of boundary forming from high-dimensional perspectives, and how robust it is in general noise mitigation.

2.1 Hypothesis: Interaction Boundary is Shifted from Orthogonal Boundary

We first elaborate on the gap extent between the positive and negative sides kept by the orthogonal boundary. Then, we present the reasoning behind the hypothesis that the intersection boundary in Figure. 1 is a shifted orthogonal boundary in the cone space.

The orthogonal boundary largely separates the positive and negative sides. High-dimensional orthogonality is a general phenomenon caused by dimension disaster, where the angles between randomly selected vectors typically approximate 90 degrees, suggesting the cosine similarity that trends toward zero. For instance, in a 1024-dimensional space, the probability of two random vectors having a cosine similarity within $[-0.1, 0.1]$ is approximately 99.86% (details are provided in Appendix. C.1). In this case, a natural boundary of cosine similarity zero forms, capably separating the positive side and negative side with a huge gap.

Cone effect may induce orthogonal boundary shift. Recent literature [14–16] has demonstrated that the cone effect is a general phenomenon in deep neural networks, where the learned embedding subspace forms a narrow cone and the orthogonal boundary encounters a positive shift. Based on this, a hypothesis is that the interaction boundary in Figure. 1 is the shifted orthogonal boundary. To prove this, we simulate the process of selecting random vectors in high-dimensional space and randomly generate thousands of pairs mapped into the shared embedding space. We find that all similarity of these random vector pairs tends to a fixed value, with the low-variance cosine similarity almost lying in the middle of clean and noise distributions (see Table. 1). An interesting phenomenon is that if we compare the mean with the intersection points in Figure. 1c-1f, we find they are almost exactly the same. This suggests that the interaction boundary is highly likely to be a shifted orthogonal boundary in cone space.

Table 1: The mean and variance of cosine similarity between randomly generated pairs.

Model	Mean	Var
CLIP	0.215	0.024
ALIGN	0.087	6e-4

2.2 Theoretical verification of the Interaction Boundary Origin

Here, we theoretically investigate whether the origin of the interaction boundary is a shifted orthogonal boundary. We first show that (i) contrastive learning separates clean and noisy samples on opposite sides of the orthogonal boundary and (ii) The relative relationships of pairs' cosine similarity stays unchanged after transmitting into the narrow cone space. Based on (i) and (ii), we can confirm that the intersection boundary at the center of the clean and noisy distributions is the shifted orthogonal boundary.

Contrastive learning empowers the separation of clean and noisy samples. For an initialized model intending to learn an embedding space, both clean and noisy samples are treated as orthogonal

random vectors since lacking semantic perception ability in the initial space. During contrastive training process, given N sample pairs $\{(x_i, y_i)\}_{i=1}^N$, the embedding space is optimized through the cross-entropy loss (Eq. 1).

$$\mathcal{L}_{ce} = \frac{1}{N} \sum_{i=1}^{N} \log \frac{\exp(m_{ii})}{\sum_{j=1}^{N} \exp(m_{ij})}, \tag{1}$$

where $M \in \mathbb{R}^{N \times N}$ represents the cosine similarity matrix of N sample pairs during training process. Each element $m_{ij} \in M$ denote the cosine similarity between x_i and y_j. The diagonal elements m_{ii} denote the cosine similarities of positive pairs, while the non-diagonal elements m_{ij} represent the cosine similarities of negative pairs.

To minimize $\mathcal{L}_{ce}$ during training, two subprocesses occur: the diagonal elements of the matrix (*i.e.*, clean pairs) are optimized to the positive side of the orthogonal boundary, while the non-diagonal elements (equivalent to noise pairs) are optimized to the negative side. Consequently, the distributions of these two types of samples are on opposite sides of the orthogonal boundary.

Relative relationship unchanged in transmitting process. We study how the boundary shifts from the entire space to the narrow cone in the neural network. The following theorem shows that the cosine similarity will be proportionally scaled to the target narrow cone, while still maintaining a boundary with properties similar to the orthogonal boundary. In other words, vectors with cosine similarity smaller than the orthogonal boundary in the original space remain smaller than the shifted boundary in the narrow cone space, while those larger remain larger.

Theorem 1 (Proportional shift of boundary). *Let $\mathbb{R}^{d_{in}}$ be the original space before being transmitted in a neural network. Suppose $u, v \in \mathbb{R}^{d_{in}}$ are any two random vectors with $\cos(u, v) \approx 0$. $u_c, v_c \in \mathbb{R}^{d_{in}}$ is a pair of clean vectors with $\cos(u_c, v_c) > 0$, while $u_n, v_n \in \mathbb{R}^{d_{in}}$ is a noisy pair with $\cos(u_n, v_n) < 0$. Given a Neural Network $F(x) = f_t(f_{t-1}(\dots f_2(f_1(x)))) \in \mathbb{R}^{d_{out}}$ with t layers. $f_i(x) = \sigma_i(\mathbf{W}_i x + \mathbf{b}_i)$ denotes i^{th} layer, where $\sigma(\cdot)$ indicates activation function. $\mathbf{W}_i \in \mathbb{R}^{d_{out}^i \times d_{in}^i}$ is a random weight matrix where each element $\mathbf{W}_i^{k,l} \sim \mathcal{N}(0, 1/d_{out}^i)$ for $k \in [d_{out}^i]$, $l \in [d_{in}^i]$, and $\mathbf{b}_i \in \mathbb{R}^{d_{out}^i}$ is a random bias vector such that $\mathbf{b}_i^k \sim \mathcal{N}(0, 1/d_{out}^i)$ for $k \in [d_{out}^i]$. Then, there always be a boundary β, satisfying:*

$$\cos(F(u_n), F(v_n)) < \cos(F(u), F(v)) \approx \beta < \cos(F(u_c), F(v_c)). \tag{2}$$

Theorem. 1 shows that the relative relationship of pairs in the original entire space, will not change after transmitting to the narrow cone space of the trained model, and there is always a boundary β concentrated on most random vectors. In Appendix. C.2, we provide a detailed statement and proof of the Theorem.

2.3 Qualitative analysis of robustness and applicability

Next, we perform a qualitative analysis to explore (i) the robustness and generality of the boundary in distinguishing between clean and noisy samples, and (ii) how the boundary's properties can be leveraged to achieve more reasonable and precise overlap handling.

How about the boundary robustness even in unfamiliar domains? Although the boundary's ability to distinguish clean and noisy samples is proven, its robustness and generality still require further exploration. For practical pre-training, it must maintain accuracy and robustness even in unfamiliar domain datasets. Since the capabilities of the pre-trained model are difficult to quantify, we conduct a qualitative analysis from the perspective of pre-trained model inference. The models pre-trained on millions of samples already possess somewhat semantic understanding capabilities. Given a positive pair from an unseen domain, due to the contrastive learning process during pre-training, it still has a strong likelihood of moving toward the positive side of the boundary, while the negative pair tends toward the negative side. Although the cosine similarity difference might be slight, as we have shown in Section. 2.1, the boundary constructs a significant gap from the perspective of high-dimensional orthogonality.

How to handle the overlaps through imbalanced probability? Due to the properties of orthogonal boundary, as cosine similarity decreases and approaches zero from the positive side, the probability

of positive samples sharply decreases. Therefore, we can design a scoring function to annotate the cleanliness of samples. This function should satisfy two requirements: for samples with cosine similarity less than or equal to zero, which are almost certainly noise, the function should assign them a weight of zero. For samples with cosine similarity greater than zero, the function gradient should increase rapidly as the cosine similarity moves further from zero.

3 Method

In this section, we present our One-Step Anti-Noise (OSA) paradigm with a workflow shown in Figure. 2. We first define the pair-based noise mitigation tasks for image-text matching, image classification, and image retrieval tasks in Sec. 3.1. Consequently, the detailed description of OSA is clarified in Sec. 3.2.

3.1 Task Definition

Let $\mathcal{D} = \{(x_i, y_i, c_i)\}_{i=1}^N$ denote a paired dataset, where (x_i, y_i) represents the i-th pair in the dataset, and c_i indicates a noise label for that pair. Specifically, when $c_i = 0$, (x_i, y_i) forms a correct (paired) match, while $c_i = 1$ denotes an incorrect (unpaired) match. The objective of noise mitigation in contrastive learning is to construct a shared embedding space that brings x_i and y_i closer when $c_i = 1$. In different tasks, x_i and y_i are distinct data types. For instance, in the image-text retrieval task, x_i and y_i represent images and texts, respectively. In the image classification task, x_i and y_i represent images and categories, respectively. In the image retrieval task, x_i and y_i represent images and relevant images, respectively. The paired sample (x, y) could be encoded into a shared embedding space by corresponding encoders $\phi_x(\cdot)$ and $\phi_y(\cdot)$. Afterward, the cosine similarity $s(x, y)$ is calculated through Eq. 3 as semantic relevance of (x, y) to guide the training.

$$s(x, y) = \frac{\phi_x(x)}{\|\phi_x(x)\|} \cdot \frac{\phi_y(y)}{\|\phi_y(y)\|}. \tag{3}$$

3.2 One-step Anti-Noise

The workflow of our noise mitigation approach OSA is depicted in Figure. 2. Initially, we utilize an estimator model to encode the input pair to a shared embedding space and continue to compute the cosine similarity between the paired embedding. Afterward, the cosine similarity is converted to a cleanliness score $w_i, (0 \leq w_i \leq 1)$ through a scoring function designed based on orthogonal properties (Section. 2.3). This score quantifies the clean degree of the sample, the smaller w_i is, the noisier the sample.

During the target model training phase, this cleanliness score is used as a weight, directly multiplied by the loss of the corresponding sample to facilitate selective learning. This noise mitigation process, being solely dependent on the estimator model, is readily adaptable to the training of various target models by simply adding an extra coefficient to the loss function, ensuring the model-agnostic property. Therefore, the key of our noise mitigation approach revolves around the estimator model and noise score assessment.

3.2.1 Estimator Model

Estimator model selection. In our approach, the Estimator Model must satisfy two critical requirements: 1) effectively mapping input pairs into a unified embedding space and 2) possessing basic semantic understanding capabilities. To meet these requirements, we employ CLIP [8], a commonly used multimodal pre-trained models, as our estimator model. It is equipped with a text encoder $\phi_t(\cdot)$ and an image encoder $\phi_v(\cdot)$, enabling it to perform basic zero-shot tasks efficiently.

Domain adaptation (Optional). While we have performed a qualitative analysis of the zero-shot pre-trained model's robustness on out-of-domain data in Section. 2.3, and shown strong robustness for edge cases in Figure. 1, considering the domain diversity in real-world scenarios, we provide an optional Domain Adaptation (DA) approach to enhance the estimator model's adaptability when encountering edge domains. Following NPC [2], we first employ a Gaussian Mixture Model (GMM) coupled with strict selection thresholds to ensure the absolute cleanliness of the chosen samples.
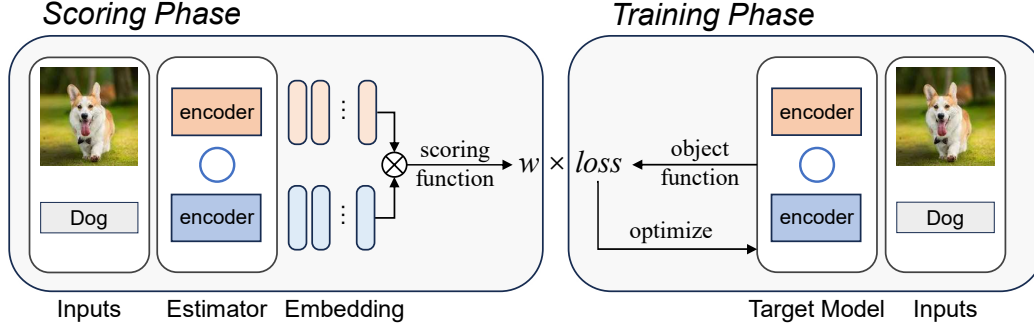
Figure 2: The workflow of OSA. In the anti-noise process, there are two phases: Scoring Phase and Training Phase. In the Scoring Phase, a pair is mapped to a shared embedding space by estimators. Then the cosine similarity is transformed to a weight w by a scoring function. In the Training Phase, the weight w is directly multiplied with the loss to instruct the optimization.

We afterward implement a warm-up phase with few steps, allowing the estimator model to better understand the semantics of the target domain. Notably, this trick is only optional for our methods. Through multiple experiments, we found that even without domain adaptation, the zero-shot CLIP model performs exceptionally well across various scenarios.

3.2.2 Noise Score Assessment

Spatial Debiasing. The cone effect phenomenon has been demonstrated as a general phenomenon for deep neural networks, typically resulting in a narrow embedding space that causes a shift of space center to a narrow cone center [14]. Specifically, when paired randomly generated inputs are mapped into a shared embedding space through model encoders, the resultant vectors exhibit an average cosine similarity that deviates from zero and tends to another fixed angle. To counteract this shift and mitigate its impact on the estimator's ability to accurately recognize noises through high-dimensional orthogonality, a random sampling method is developed. We begin by constructing K random sample pairs $\mathcal{R} = \{(x_j, y_j) \mid j = 1, 2, \ldots, K\}$ and processing them through the estimator's encoder to generate a set of vectors. Then the average cosine similarity among these vectors will be calculated as the space shift β through:

$$\beta = \frac{\sum_{j=1}^{K} s(x_j, y_j)}{K}. \tag{4}$$

Scoring Function. After spatial debiasing, we employ a scoring function $w(\cdot)$ to evaluate the cleanliness of the input pair (x, y). In section. 2.3, we have elaborate how to handle overlaps based on the orthogonal boundary property. For an estimator model trained on millions of samples using contrastive learning, clean pairs (diagonal elements) are optimized to positive side, while noise pairs (non-diagonal elements) are optimized to negative side. Given unfamiliar pairs, the model also tends to map clean pairs towards positive and noisy pairs towards negative. Despite the potentially slight similarity difference between clean and noisy pairs, high-dimensional orthogonality ensures a substantial gap between them. In this case, a negative cosine similarity $s(x, y)$ computed by the estimator, indicating the pair is almost certainly noise, should be assigned a score of zero. For samples with $s(x, y)$ greater than zero, the probability of the sample being positive sharply decreases as the cosine similarity approaches zero from the positive side. Therefore, the function gradient should increase rapidly as the cosine similarity moves further from zero. To systematically score the noise, we design the scoring function as:

$$w(x, y, \beta) = \begin{cases} 0 & , s(x, y) - \beta \leq 0 \\ -(s(x, y) - \beta)^2 (s(x, y) - \beta - 1) & , otherwise \end{cases} \tag{5}$$

Re-weight Training. After scoring, the target model can selectively learn from the samples by re-weighting the loss. Noise samples with smaller weights will have a reduced impact on model updates and will be effectively mitigated. For a sample (x, y), let $\mathcal{L}_{x,y}$ denote its loss, the re-computed loss

6

$\mathcal{L}_{re}$ is defined as:

$$\mathcal{L}_{re} = w(x, y, \beta) \times \mathcal{L}_{x,y}. \tag{6}$$

4 Experiments

In this section, we present experiments on multiple datasets with label noise, demonstrating the effectiveness of our methods. Firstly, we describe the datasets, metrics, and implementation details. Then, we report our results on several downstream tasks. Lastly, we conduct ablation studies to show how each part of our method contributes and examine how these parts interact. The literature involved in our experiments and richer related work are detailed in Appendix. B.

4.1 Evaluation Setting

In this section, we briefly introduce the datasets and evaluation metrics used in the experiments. For more dataset and implementation details, please refer to Appendix. A.

Datasets. We evaluate our method on three downstream tasks with noisy labels, including one multimodal task and two visual tasks. For the cross-modal matching task, we perform experiments on the MSCOCO [12] and Flickr30K [17] datasets. Following NPC [2], we further carry out evaluations on a real-world noisy dataset CC120K. For image classification tasks, experiments are conducted under three subsets of WebFG-496 [3]—Aircraft, Bird, and Car. For image retrieval tasks, we conduct experiments on the CARS98N dataset under PRISM [5] setting.

Evaluation Metrics. For the image-text matching task, the recall value of the top-K retrieved results (R@K) is used. For classification tasks, accuracy serves as the evaluation metric. For the image retrieval task, we use Precision@1 and mAP@R for evaluation.

4.2 Comparisons with State of The Arts

Table 2: Comparison on noisy MS-COCO.

| Noise ratio | Method | MS-COCO 1K | | | | | | MS-COCO 5K | | | | | |
| | | i2t | | | t2i | | | i2t | | | t2i | | |
		R@1	R@5	R@10	R@1	R@5	R@10	R@1	R@5	R@10	R@1	R@5	R@10
0%	VSE∞	82.0	**97.2**	98.9	69.0	92.6	96.8	62.3	87.1	**93.3**	48.2	**76.7**	85.5
	PCME++	81.6	**97.2**	99.0	**69.2**	**92.8**	97.1	62.1	86.8	**93.3**	48.1	**76.7**	**85.5**
	PAU	80.4	96.2	98.5	67.7	91.8	96.6	63.6	85.2	92.2	46.8	74.4	83.7
	NPC	**82.2**	96.5	**98.7**	68.3	92.0	**98.7**	65.4	**87.3**	93.1	48.5	75.4	84.4
	CLIP	80.1	95.7	98.2	67.1	91.4	96.6	62.9	84.9	91.6	46.5	73.8	82.9
	+OSA	**82.2**	96.5	**98.7**	68.8	92.1	96.7	**65.6**	86.8	92.9	**49.1**	76.2	84.8
	ALIGN	84.9	97.3	**99.0**	70.5	92.8	97.2	69.6	**89.9**	94.5	50.5	77.5	85.7
	+OSA	**85.3**	**97.4**	**99.0**	**71.4**	**93.1**	97.3	**69.8**	**89.9**	94.8	**51.4**	**78.2**	**86.3**
20%	VSE∞	78.4	94.3	97.0	65.5	89.3	94.1	58.6	83.4	89.9	45.0	72.9	81.7
	PCME++	78.4	95.9	98.4	64.9	90.8	96.1	57.7	83.9	91.0	43.2	72.3	82.4
	PAU	78.2	95.2	98.1	64.5	90.0	95.4	59.3	82.9	90.4	44.2	71.3	81.3
	NPC	79.9	95.9	98.4	66.3	90.8	**98.4**	61.6	85.4	91.6	46.0	73.4	82.9
	CLIP	76.0	94.3	97.5	63.4	89.0	94.8	55.3	79.1	86.9	41.0	68.8	79.3
	+OSA	**81.6**	**96.2**	**98.5**	**68.9**	**92.0**	96.6	**65.8**	**86.4**	**92.5**	**48.7**	**76.1**	**84.5**
	ALIGN	79.4	95.7	98.2	66.2	90.8	96.1	60.9	84.5	91.0	46.3	73.6	82.3
	+OSA	**85.1**	**97.4**	**99.1**	**70.9**	**93.0**	97.3	**69.7**	**90.0**	**94.7**	**50.9**	**77.8**	**86.2**
50%	VSE∞	44.3	76.1	86.9	34.0	69.2	84.5	22.4	48.2	61.1	15.8	38.8	52.1
	PCME++	74.8	94.3	97.7	60.4	88.7	95.0	52.5	79.6	88.4	38.6	68.0	79.0
	PAU	76.4	94.1	97.6	62.3	88.5	94.6	57.3	81.5	88.8	41.9	69.4	79.6
	NPC	78.2	94.4	97.7	63.1	89.0	**97.7**	59.9	82.9	89.7	43.0	70.2	80.0
	CLIP	73.9	93.0	97.2	60.1	87.3	94.0	54.1	78.5	86.6	39.7	67.2	77.5
	+OSA	**80.4**	**96.2**	**98.6**	**67.8**	**91.6**	96.4	**64.0**	**85.5**	**91.9**	**47.9**	**74.6**	**83.8**
	ALIGN	78.0	95.8	98.5	65.4	90.3	96.0	60.1	84.3	91.2	45.2	72.8	82.1
	+OSA	**84.3**	**97.0**	**98.9**	**70.0**	**92.5**	97.0	**68.5**	**89.2**	**94.2**	**50.0**	**77.0**	**85.4**

Results on MSCOCO. To fairly demonstrate the effectiveness of our method, we compare OSA with various robust learning image-text matching approaches using the same ViT-B/32 CLIP as

backbone, including VSE∞ [18], PCME++ [19], PAU [20], NPC [2]. Besides, we separately employ OSA on both CLIP [8] and ALIGN [11]. The results in Table. 2 show that OSA outperforms all previous approaches on all metrics with a huge gap. In the more challenging MS-COCO 5K set with 50% noise ratio, OSA surpasses the SOTA method NPC in the R@1 for both image-to-text (i2t) and text-to-image (t2i) matching by 8.6% and 7.0%, respectively. Another phenomenon is that as the noise ratio increases from 0% to 50%, all other methods encounter severe performance drop, with an averaging drop of 5.05% for NPC across four R@1 metrics. In contrast, OSA exhibits only a slight decrease of 1.275%, showcasing the accuracy and robustness of OSA in anti-noise tasks.

Table 3: Comparison on noisy Flickr30K.

Method	Noise ratio	i2t R@1	R@5	R@10	t2i R@1	R@5	R@10	Noise ratio	i2t R@1	R@5	R@10	t2i R@1	R@5	R@10
NCR	0%	77.3	94.0	97.5	59.6	84.4	89.9	20%	73.5	93.2	96.6	56.9	82.4	88.5
DECL		79.8	94.9	97.4	59.5	83.9	89.5		77.5	93.8	97.0	56.1	81.8	88.5
BiCro		81.7	95.3	98.4	61.6	85.6	90.8		78.1	94.4	97.5	60.4	84.4	89.9
NPC		87.9	**98.1**	**99.4**	75.0	**93.7**	**97.2**		87.3	97.5	98.8	72.9	92.1	95.8
CLIP		86.2	97.6	99.2	72.9	92.3	96.0		82.3	95.5	98.3	66.0	88.5	93.5
+OSA		**88.6**	97.7	99.3	**75.6**	93.6	96.8		**88.9**	**97.7**	**99.1**	**75.6**	**93.3**	**96.9**
NCR	40%	68.1	89.6	94.8	51.4	78.4	84.8	60%	13.9	37.7	50.5	11.0	30.1	41.4
DECL		72.7	92.3	95.4	53.4	79.4	86.4		65.2	88.4	94.0	46.8	74.0	82.2
BiCro		74.6	92.7	96.2	55.5	81.1	87.4		67.6	90.8	94.4	51.2	77.6	84.7
NPC		85.6	97.5	98.4	71.3	91.3	95.3		83.0	95.9	98.6	68.1	89.6	94.2
CLIP		76.2	93.3	96.5	59.4	85.0	90.9		66.3	87.3	93.0	52.1	78.8	87.4
+OSA		**87.3**	**97.6**	**99.3**	**74.2**	**93.1**	**96.7**		**87.2**	**98.1**	**99.6**	**74.4**	**92.9**	**96.4**

Results on Flickr30K. To further demonstrate the generalization ability of OSA, we evaluate on the Flickr30K dataset and compare with several anti-noise methods, including NCR [1], DECL [9], BiCro [7], and NPC [2]. The results are presented in Table. 3 of Appendix. It is evident that OSA consistently outperforms all models on the R@1 metric. Notably, compared with the baseline CLIP, training with OSA at a 60% noise ratio achieves 20.9% R@1 improvement for i2t and a 22.3% R@1 improvement in t2i, further indicating the effectiveness of OSA on noise mitigation. Additionally, OSA demonstrates similar noise robustness on the Flickr30K dataset as observed on MSCOCO, with only 1.4% R@1 drop on i2t and 1.2% R@1 drop on t2i ranging from 0% noise to 60% noise, while all of the other anti-noise approaches hardly resist the detriment from high-ratio noise. All of these results demonstrate the effectiveness and robustness of OSA on anti-noise tasks.

Results on CC120K. To further verify the reliability of OSA in real scenarios, we conduct evaluations on a large-scale real-world noisy dataset, CC120K, with 3%-20% noise ratio. The results shown in Table. 4 indicate that OSA outperforms the current state-of-the-art method NPC, even in larger-scale real-world domains. This demonstrates the feasibility and generality of OSA even in practical training scenarios.

Table 4: Comparison on real-world noisy dataset CC120K.

Method	i2t R@1	R@5	R@10	t2i R@1	R@5	R@10
NPC	71.1	92.0	**96.2**	73.0	90.5	**94.8**
CLIP	68.8	87.0	92.9	67.8	86.4	90.9
+OSA	**73.1**	**92.2**	95.7	**73.9**	**91.2**	94.7

Table 5: Results of other image-based tasks.

Method	Image Classification Aircraft Acc	Bird Acc	Car Acc	Image Retrieval Prec.	mAP
Baseline	65.44	62.29	75.90	71.69	18.16
+OSA	**73.18**	**70.50**	**80.19**	**78.45**	**24.99**

Results on Other Downstream Tasks. To validate the transferability of OSA across different tasks, we evaluate it on two additional tasks: image classification and image retrieval. The results are presented in Table. 5. The baseline method for both tasks leverages contrastive learning. In the image classification task, OSA outperforms the baseline by 7.74%, 8.21%, and 4.28% on the Aircraft, Bird, and Car subsets, respectively. In the image retrieval task, OSA improves performance by 6.76% in precision and 6.83% in mAP. These improvements demonstrate the strong task transferability and generality of OSA.

Table 6: The results of the target model with different architectures on noisy MSCOCO.

Noise ratio	Method	Architecture	MS-COCO 1K						MS-COCO 5K					
			i2t			t2i			i2t			t2i		
			R@1	R@5	R@10	R@1	R@5	R@10	R@1	R@5	R@10	R@1	R@5	R@10
0%	Baseline	ResNet-152	58.9	**86.9**	**93.8**	44.2	77.9	**88.3**	34.9	**64.3**	**76.1**	23.3	**50.9**	**64.2**
	+OSA		58.9	86.2	93.7	**44.3**	77.9	87.9	**35.0**	64.1	76.0	**23.5**	50.8	63.9
	Baseline	VGG-19	49.6	79.4	89.1	38.0	72.9	**84.7**	**26.9**	54.2	66.8	18.7	43.8	56.8
	+OSA		50.1	80.0	89.3	38.3	73.0	84.6	26.6	54.4	67.4	18.8	43.9	57.3
20%	Baseline	ResNet-152	45.8	70.3	83.7	36.1	68.4	79.7	26.0	48.4	58.3	18.3	42.0	54.0
	+OSA		58.1	86.1	93.2	43.4	76.8	87.2	33.7	62.6	74.5	22.5	49.7	62.8
	Baseline	VGG-19	33.2	67.1	81.5	25.9	58.0	71.4	13.7	35.0	49.2	10.7	29.9	41.9
	+OSA		49.3	79.1	88.6	37.2	71.9	83.8	25.2	53.3	65.3	17.9	42.6	55.9
50%	Baseline	ResNet-152	28.4	61.2	75.2	5.2	14.0	19.5	11.0	31.0	43.6	1.6	6.0	9.2
	+OSA		55.0	84.0	92.0	40.7	74.7	85.6	30.8	60.2	72.3	20.9	46.6	60.0
	Baseline	VGG-19	2.5	9.8	16.2	0.1	0.5	1.0	0.5	2.5	4.4	0.0	0.1	0.2
	+OSA		47.1	77.7	87.6	35.7	70.3	82.8	24.0	51.5	64.0	16.9	40.8	54.2

4.3 Target Model-Agnostic Analysis

OSA is an architecture-agnostic paradigm that can be easily adapted to various models. To verify its model-agnostic property, we evaluate it across models with different architectures. Subsequently, we apply it to other anti-noise models to demonstrate its generalization capability in noise mitigation.

Architecture-agnostic Analysis. The effectiveness of OSA on Vision Transformer (ViT) has been proven in Section. 4.2. We further explore the generality of OSA on target models with other architectures. Specifically, we deploy OSA above the VSE++ [21] model with two different architecture types: ResNet-152 [22] and VGG-19 [23]. These two architectures have revealed significant sensitivity and vulnerability to noise [1]. In this experiment, all estimator models employ zero-shot CLIP and we utilize the original VSE++ as our baseline. The results in Table. 6 indicate a significant performance degradation emerged for the baseline methods in noisy setting, while a stable performance is achieved after employing OSA. The stable performance on these two noise-vulnerable architectures fully demonstrates that OSA possesses the architecture-agnostic property.

Table 7: The results of other methods employing OSA on MSCOCO 1K.

Noise Ratio	Method	i2t			t2i		
		R@1	**R@5**	**R@10**	**R@1**	**R@5**	**R@10**
0%	NPC	82.2	**96.5**	**98.7**	68.3	**92.0**	**98.7**
	+OSA	**82.4**	96.4	98.6	**68.5**	91.8	**98.7**
20%	NPC	79.9	95.9	98.4	66.3	90.5	98.4
	+OSA	**81.2**	**96.0**	**98.6**	**66.9**	**91.2**	**98.6**
50%	NPC	78.2	94.4	97.7	63.1	89.0	97.7
	+OSA	**79.3**	**95.6**	**98.2**	**66.8**	**90.8**	**98.2**

Adaptability to Other Anti-Noise Models. Theoretically, OSA can be adapted to any target model, providing noise resistance. However, can OSA further enhance the robustness of models specifically designed for noise mitigation? To investigate this, we applied OSA to the current state-of-the-art model, NPC [2]. As shown in Table. 7 of Appendix, even for noise-mitigating models, OSA consistently improves training robustness. This finding further demonstrates the broad adaptability of OSA across different model types.

4.4 Estimator Model Analysis.

The estimator model is the basis of OSA's anti-noise capability. In this section, we explore the impact of different estimator models on noise mitigation, and examine the impact of domain adaptation in noise mitigation. In Table. 8 of Appendix, we investigate four types of estimators: "None" refers to training CLIP directly without using OSA. "CLIP (w/o DA)" and "ALIGN (w/o DA)" represent using CLIP and ALIGN without domain adaptation as estimators, respectively, *i.e.*, zero-shot CLIP and ALIGN. "CLIP (w DA)" indicates the CLIP with domain adaptation. The target models are all CLIP.

We can observe that both of CLIP and ALIGN as estimators significantly enhance the target model performance stability when learning with noise, indicating that the choice of estimator is very flexible. Both CLIP and ALIGN demonstrate exceptional performance when served as estimators. The other phenomenon is that the zero-shot CLIP model shows comparable performance to the domain-adapted CLIP with a even better performance at lower noise ratios. This indicates that zero-shot CLIP, as an estimator, already performs exceptionally well in noise mitigation. The domain adaptation is unnecessary. This further enhances the deployment convenience of OSA.

Table 8: Ablation study of estimator type on noisy MS-COCO.

| Noise ratio | Estimator | MS-COCO 1K | | | | | | MS-COCO 5K | | | | | |
| | | i2t | | | t2i | | | i2t | | | t2i | | |
		R@1	R@5	R@10	R@1	R@5	R@10	R@1	R@5	R@10	R@1	R@5	R@10
0%	None	80.1	95.7	98.2	67.1	91.4	96.6	62.9	84.9	91.6	46.5	73.8	82.9
	CLIP (w/o DA)	**82.6**	**96.7**	98.7	68.5	**92.1**	**96.7**	**66.2**	**87.0**	**93.3**	48.6	75.7	**84.8**
	ALIGN (w/o DA)	81.9	96.7	98.7	68.9	92.2	96.9	64.8	86.6	92.7	49.0	75.9	84.7
	CLIP (w DA)	82.2	96.5	98.7	**68.8**	92.1	96.7	65.6	86.8	92.9	**49.1**	**76.2**	**84.8**
20%	None	76.0	94.3	97.5	63.4	89.0	94.8	55.3	79.1	86.9	41.0	68.8	79.3
	CLIP (w/o DA)	**81.8**	96.1	**98.7**	68.2	91.9	96.5	64.8	**86.6**	92.3	48.3	75.4	84.1
	ALIGN (w/o DA)	81.2	96.0	98.6	67.7	91.5	96.4	64.8	86.2	92.3	47.8	74.9	83.9
	CLIP (w DA)	81.6	**96.2**	98.5	**68.9**	**92.0**	**96.6**	**65.8**	86.4	**92.5**	48.7	**76.1**	**84.5**
50%	None	73.9	93.0	97.2	60.1	87.3	94.0	54.1	78.5	86.6	39.7	67.2	77.5
	CLIP (w/o DA)	79.6	95.6	98.4	65.9	90.8	95.9	62.4	84.8	90.8	45.7	73.1	82.5
	ALIGN (w/o DA)	80.4	95.6	98.3	66.0	90.5	95.8	62.0	84.9	91.8	45.7	73.2	82.5
	CLIP (w DA)	**80.4**	**96.2**	**98.6**	67.8	**91.6**	**96.4**	**64.0**	**85.5**	**91.9**	47.9	74.6	83.8

4.5 Noise Assessment Accuracy

Noise Detection Accuracy Analysis. To figure out how accurate OSA is in recognizing noise, we evaluate the accuracy and recall on CLIP without Domain-Adaptation (w/o DA) and CLIP with Domain-Adaptation (w DA) on noisy MSCOCO. We utilize zero as the threshold to roughly divide pairs into noise and clean sets, respectively. Concretely, we classify scores less than or equal to 0 as noise, and scores greater than 0 as clean. The Accuracy means the proportion of the clean pairs correctly classified into the clean set, while the Recall indicates the noisy pairs correctly classified into the noisy set. The results presented in Table. 10 indicates the powerful noise recognizing capability of OSA. The remarkable performance on CLIP (w/o DA) fully demonstrates the generality of OSA. Another notable phenomenon is that all recall scores converge towards 100, indicating that OSA achieves greater accuracy in noise detection. This suggests that OSA can almost entirely eliminate the impact of noise on training.

Table 9: Mean Noise Rank Comparison between OSA and NPC.

Noise Ratio	Method	Mean Noise Rank↑	Optimal Rank	Noise Number	Sample Number
20%	NPC	1641.3	1815.5	370	2,000
	OSA	**1809.1**	1815.5	370	2,000
50%	NPC	1456.2	1524.0	953	2,000
	OSA	**1520.7**	1524.0	953	2,000

Noise Re-weighting Accuracy Comparison. Some anti-noise methods, like NPC, also employ loss re-weighting for optimization. To assess whether our method assigns relatively smaller weights to noise than these methods, we first analyze the weights generated by NPC and OSA. Due to differences in weight scales across methods, a direct comparison is unfair. Therefore, to unify the scale, we adopt a ranking-based approach, sorting weights in descending order and calculating the Mean Noise Rank. This metric evaluates whether smaller weights are consistently assigned to noisy samples relative to clean ones. Our experiments use 2,000 randomly selected samples from the MSCOCO dataset under two noise conditions: 20% noise (370 noisy samples) and 50% noise (953 noisy samples). The theoretical optimal Mean Noise Ranks, where all noisy weights are ranked last, are 1815.5 and 1524.0, respectively. Results presented in Table. 9 of Appendix show that OSA achieves a higher Mean Noise Rank compared to NPC, demonstrating greater accuracy in re-weighting. Moreover, OSA's rankings are nearly optimal (20% noise: 1809.1 for OSA versus 1815.5 optimal; 50% noise:

Table 10: ACC and recall of noise detection.

Estimator Type	Noise Ratio	Acc	Recall
CLIP (w/o DA)	0.2	93.88	97.49
CLIP (w DA)	0.2	97.68	97.18
CLIP (w/o DA)	0.5	93.91	99.35
CLIP (w DA)	0.5	98.14	99.24

Table 11: Overhead Comparison.

Model	Time	Extra Time
CLIP	97 min	0 min
NPC	323 min	226 min
OSA	118 min	21 min

1520.7 for OSA versus 1524.0 optimal). This near-perfect alignment indicates that OSA effectively places almost all noisy samples behind the clean ones.

4.6 Computational Cost Analysis

Cost in Pre-training. To evaluate the practicality of OSA in a real-world pre-training scenario, we estimate the additional computational cost for processing 1 billion data points. Using an NVIDIA RTX 3090 with an inference batch size of 4096, utilizing approximately 24 GB of GPU memory, processing the MS-COCO dataset consisting of 566,435 pairs takes approximately 153 seconds. At this inference rate, processing 1 billion data points would require approximately 75 hours on a single RTX 3090. This cost is negligible within the context of large-scale pre-training, especially when leveraging multiple GPUs for parallel inference.

Time Cost Comparison. To further examine the computational efficiency of OSA compared to other anti-noise techniques, we evaluate training time against two representative approaches: CLIP and NPC. CLIP, which serves as the baseline, is trained directly without any additional technique. NPC, the current state-of-the-art, also uses CLIP as its backbone but applies an anti-noise technique by estimating the negative impact of each sample, necessitating double backward passes. The training time comparison, presented in Table. 11, shows that our method introduces only a minimal increase in training time compared to direct training, requiring just one-tenth of the additional time needed by NPC. This highlights the efficiency of OSA, making it well-suited for large-scale robust training.

5 Conclusion

Broader Impacts. In this work, we investigated the possibility of anti-noise in practical large-scale training. We introduced a novel model-agnostic anti-noise paradigm with advantages such as task transferability, model adaptability, and low computational overhead. By leveraging the properties of high-dimensional spaces, we found a robust and effective boundary for distinguishing between noisy and clean samples. Through rigorous theoretical analysis and comprehensive experimentation, we validated the efficacy and robustness of OSA for general noise mitigation. Although our primary objective is to adapt to practical large-scale training, OSA also achieves SOTA performance in standard anti-noise settings. To the best of our knowledge, this is the first work to explore anti-noise in practical large-scale training scenarios, as well as the first to propose a general anti-noise approach.

Limitations and Future Works. Limited by the significant computational cost of pre-training, it is difficult for us to evaluate in a real pre-training process. Instead, we simulate large-scale pre-training processes to the greatest extent possible, such as evaluating on the real-world noisy dataset CC120K, which shares similar domains with mainstream pre-training datasets like CC4M and CC12M. Exploring the broad domain adaptability of OSA in real pre-training scenarios will be a valuable direction for future work.

References

[1] Zhenyu Huang, Guocheng Niu, Xiao Liu, Wenbiao Ding, Xinyan Xiao, Hua Wu, and Xi Peng. Learning with noisy correspondence for cross-modal matching. In *NeurIPS*, pages 29406–29419, 2021. 1, 2, 8, 9, 15, 16

[2] Xu Zhang, Hao Li, and Mang Ye. Negative pre-aware for noisy cross-modal matching. In *AAAI*, pages 7341–7349, 2024. 1, 2, 5, 7, 8, 9, 15, 16

[3] Zeren Sun, Yazhou Yao, Xiu-Shen Wei, Yongshun Zhang, Fumin Shen, Jianxin Wu, Jian Zhang, and Heng Tao Shen. Webly supervised fine-grained recognition: Benchmark datasets and an approach. In *ICCV*, pages 10582–10591. IEEE, 2021. 1, 7, 15

[4] Xingrui Yu, Bo Han, Jiangchao Yao, Gang Niu, Ivor W. Tsang, and Masashi Sugiyama. How does disagreement help generalization against label corruption? In *ICML*, pages 7164–7173, 2019. 1

[5] Chang Liu, Han Yu, Boyang Li, Zhiqi Shen, Zhanning Gao, Peiran Ren, Xuansong Xie, Lizhen Cui, and Chunyan Miao. Noise-resistant deep metric learning with ranking-based instance selection. In *CVPR*, pages 6811–6820, 2021. 1, 7, 15, 16

[6] Sarah Ibrahimi, Arnaud Sors, Rafael Sampaio de Rezende, and Stéphane Clinchant. Learning with label noise for image retrieval by selecting interactions. In *WACV*, pages 468–477, 2022. 1

[7] Shuo Yang, Zhaopan Xu, Kai Wang, Yang You, Hongxun Yao, Tongliang Liu, and Min Xu. Bicro: Noisy correspondence rectification for multi-modality data via bi-directional cross-modal similarity consistency. In *CVPR*, pages 19883–19892, 2023. 1, 8, 15, 16

[8] Alec Radford, Jong Wook Kim, Chris Hallacy, Aditya Ramesh, Gabriel Goh, Sandhini Agarwal, Girish Sastry, Amanda Askell, Pamela Mishkin, Jack Clark, Gretchen Krueger, and Ilya Sutskever. Learning transferable visual models from natural language supervision. In *ICML*, volume 139, pages 8748–8763, 2021. 2, 5, 8

[9] Yang Qin, Dezhong Peng, Xi Peng, Xu Wang, and Peng Hu. Deep evidential learning with noisy correspondence for cross-modal retrieval. In *ACM MM*, pages 4948–4956, 2022. 2, 8, 15

[10] Junnan Li, Richard Socher, and Steven C. H. Hoi. Dividemix: Learning with noisy labels as semi-supervised learning. In *ICLR*, 2020. 2, 16

[11] Chao Jia, Yinfei Yang, Ye Xia, Yi-Ting Chen, Zarana Parekh, Hieu Pham, Quoc V. Le, Yun-Hsuan Sung, Zhen Li, and Tom Duerig. Scaling up visual and vision-language representation learning with noisy text supervision. In *ICML*, volume 139, pages 4904–4916, 2021. 2, 8

[12] Tsung-Yi Lin, Michael Maire, Serge J. Belongie, James Hays, Pietro Perona, Deva Ramanan, Piotr Dollár, and C. Lawrence Zitnick. Microsoft COCO: common objects in context. In *ECCV*, volume 8693, pages 740–755, 2014. 2, 7

[13] Robin Rombach, Andreas Blattmann, Dominik Lorenz, Patrick Esser, and Björn Ommer. High-resolution image synthesis with latent diffusion models. In *CVPR*, pages 10674–10685, 2022. 2

[14] Weixin Liang, Yuhui Zhang, Yongchan Kwon, Serena Yeung, and James Y. Zou. Mind the gap: Understanding the modality gap in multi-modal contrastive representation learning. In *NeurIPS*, 2022. 3, 6, 17

[15] Simion-Vlad Bogolin, Ioana Croitoru, Hailin Jin, Yang Liu, and Samuel Albanie. Cross modal retrieval with querybank normalisation. In *CVPR*, pages 5184–5195, 2022.

[16] Kawin Ethayarajh. How contextual are contextualized word representations? comparing the geometry of bert, elmo, and GPT-2 embeddings. In *EMNLP*, pages 55–65, 2019. 3

[17] Peter Young, Alice Lai, Micah Hodosh, and Julia Hockenmaier. From image descriptions to visual denotations: New similarity metrics for semantic inference over event descriptions. *Trans. Assoc. Comput. Linguistics*, 2:67–78, 2014. 7

[18] Jiacheng Chen, Hexiang Hu, Hao Wu, Yuning Jiang, and Changhu Wang. Learning the best pooling strategy for visual semantic embedding. In *CVPR*, pages 15789–15798, 2021. 8

[19] Sanghyuk Chun. Improved probabilistic image-text representations. *arXiv preprint arXiv:2305.18171*, 2023. 8

[20] Hao Li, Jingkuan Song, Lianli Gao, Xiaosu Zhu, and Hengtao Shen. Prototype-based aleatoric uncertainty quantification for cross-modal retrieval. In *NeurIPS*, 2023. 8

[21] Fartash Faghri, David J. Fleet, Jamie Ryan Kiros, and Sanja Fidler. VSE++: improving visual-semantic embeddings with hard negatives. In *BMCV*, page 12, 2018. 9

[22] Kaiming He, Xiangyu Zhang, Shaoqing Ren, and Jian Sun. Deep residual learning for image recognition. In *CVPR*, pages 770–778, 2016. 9

[23] Karen Simonyan and Andrew Zisserman. Very deep convolutional networks for large-scale image recognition. *arXiv preprint arXiv:1409.1556*, 2014. 9

[24] Kuang-Huei Lee, Xi Chen, Gang Hua, Houdong Hu, and Xiaodong He. Stacked cross attention for image-text matching. In *ECCV*, volume 11208, pages 212–228, 2018. 15

[25] Yale Song and Mohammad Soleymani. Polysemous visual-semantic embedding for cross-modal retrieval. In *CVPR*, pages 1979–1988, 2019.

[26] Kunpeng Li, Yulun Zhang, Kai Li, Yuanyuan Li, and Yun Fu. Visual semantic reasoning for image-text matching. In *ICCV*, pages 4653–4661, 2019.

[27] Hao Li, Jingkuan Song, Lianli Gao, Pengpeng Zeng, Haonan Zhang, and Gongfu Li. A differentiable semantic metric approximation in probabilistic embedding for cross-modal retrieval. In *NeurIPS*, volume 35, pages 11934–11946, 2022.

[28] Haiwen Diao, Ying Zhang, Lin Ma, and Huchuan Lu. Similarity reasoning and filtration for image-text matching. In *AAAI*, pages 1218–1226, 2021. 15

[29] Xuefeng Liang, Longshan Yao, Xingyu Liu, and Ying Zhou. Tripartite: Tackle noisy labels by a more precise partition. *CoRR*, 2022. 15

[30] Kun Yi and Jianxin Wu. Probabilistic end-to-end noise correction for learning with noisy labels. In *CVPR*, pages 7017–7025, 2019. 16

[31] Zhilu Zhang and Mert R. Sabuncu. Generalized cross entropy loss for training deep neural networks with noisy labels. In *NeurIPS*, pages 8792–8802, 2018. 16

[32] Aditya Krishna Menon, Brendan van Rooyen, Cheng Soon Ong, and Bob Williamson. Learning from corrupted binary labels via class-probability estimation. In *ICML*, volume 37, pages 125–134, 2015.

[33] Nagarajan Natarajan, Inderjit S. Dhillon, Pradeep Ravikumar, and Ambuj Tewari. Learning with noisy labels. In *NeurIPS*, pages 1196–1204, 2013.

[34] Giorgio Patrini, Alessandro Rozza, Aditya Krishna Menon, Richard Nock, and Lizhen Qu. Making deep neural networks robust to label noise: A loss correction approach. In *CVPR*, pages 2233–2241, 2017.

[35] Xiaobo Xia, Tongliang Liu, Nannan Wang, Bo Han, Chen Gong, Gang Niu, and Masashi Sugiyama. Are anchor points really indispensable in label-noise learning? In *NeurIPS*, pages 6835–6846, 2019.

[36] Aritra Ghosh, Himanshu Kumar, and P. S. Sastry. Robust loss functions under label noise for deep neural networks. In *Proceedings of the Thirty-First AAAI Conference on Artificial Intelligence, February 4-9, 2017, San Francisco, California, USA*, pages 1919–1925. AAAI, 2017.

[37] Xinshao Wang, Yang Hua, Elyor Kodirov, David A Clifton, and Neil M Robertson. Imae for noise-robust learning: Mean absolute error does not treat examples equally and gradient magnitude's variance matters. *arXiv preprint arXiv:1903.12141*, 2019.

[38] Yisen Wang, Xingjun Ma, Zaiyi Chen, Yuan Luo, Jinfeng Yi, and James Bailey. Symmetric cross entropy for robust learning with noisy labels. In *ICCV*, pages 322–330, 2019.

[39] Yilun Xu, Peng Cao, Yuqing Kong, and Yizhou Wang. L_dmi: A novel information-theoretic loss function for training deep nets robust to label noise. In *NeurIPS*, pages 6222–6233, 2019.

[40] Zhilu Zhang and Mert R. Sabuncu. Generalized cross entropy loss for training deep neural networks with noisy labels. In *NeurIPS*, pages 8792–8802, 2018. 16

[41] Zeren Sun, Fumin Shen, Dan Huang, Qiong Wang, Xiangbo Shu, Yazhou Yao, and Jinhui Tang. PNP: robust learning from noisy labels by probabilistic noise prediction. In *CVPR*, pages 5301–5310, 2022. 16

[42] Paul Albert, Eric Arazo, Tarun Krishna, Noel E. O'Connor, and Kevin McGuinness. Is your noise correction noisy? PLS: robustness to label noise with two stage detection. In *WACV*, pages 118–127, 2023.

[43] Yazhou Yao, Zeren Sun, Chuanyi Zhang, Fumin Shen, Qi Wu, Jian Zhang, and Zhenmin Tang. Jo-src: A contrastive approach for combating noisy labels. In *CVPR*, pages 5192–5201, 2021. 16

[44] Paul Albert, Diego Ortego, Eric Arazo, Noel E. O'Connor, and Kevin McGuinness. Addressing out-of-distribution label noise in webly-labelled data. In *WACV*, pages 2393–2402, 2022. 16

[45] Dong Wang and Xiaoyang Tan. Robust distance metric learning via bayesian inference. *IEEE Trans. Image Process.*, 27(3):1542–1553, 2018. 16

[46] Xinlong Yang, Haixin Wang, Jinan Sun, Shikun Zhang, Chong Chen, Xian-Sheng Hua, and Xiao Luo. Prototypical mixing and retrieval-based refinement for label noise-resistant image retrieval. In *ICCV*, pages 11205–11215, 2023. 16

[47] Sarah Ibrahimi, Arnaud Sors, Rafael Sampaio de Rezende, and Stéphane Clinchant. Learning with label noise for image retrieval by selecting interactions. In *WACV*, pages 468–477, 2022. 16

Appendix

A Details of Implementation and Datasets

Dataset Details. MSCOCO is widely used for noisy cross-modal matching, with each image accompanied by five descriptive captions. Following the setting of [1], we utilize 113,287 images for training, 5,000 for validation, and 5,000 for testing. The Flickr30K dataset encompasses 31,783 image-text instances, each image paired with five textual annotations. Adhering to the NCR [1], we use 29,783 images for training and 1,000 images each for validation and testing. Regarding noise splits, following the NCR categorization, we conduct experiments at noise ratios of 0%, 20%, 40%, and 60%. CC120K is a real-world multimodal noisy dataset collected by [2] from the Internet, with about 3%-20% noise ratio. There are 118,851 image-text pairs for training, 1,000 for validation, and 1,000 for testing.

The Aircraft, Bird, and Car we used in the image classification task are three non-overlapping subsets of the WebFG-496 [3] dataset. WebFG-496 consists of 53,339 images, totaling 496 subcategories. This dataset is annotated using a webly supervised approach, which leverages resources from web search engines (*e.g.*, Google Image Search Engine, Bing Image Search Engine) to expand the annotated image dataset.

For the image retrieval task, we conduct experiments on the CARS98N dataset under PRISM's setting [5]. We utilize 9,558 car-related images sourced from text-based searches on Pinterest as the training set, and employ the remaining 98 categories from CARS, unsearched on Pinterest, as a clean test set. The dataset's noise is inherently real-world, with its creators estimating a noise ratio of approximately 50%.

Implementation Details. To demonstrate the effectiveness of the OSA, we incorporate an estimator, built around the core of CLIP, and re-weighting operations based on the Estimator's outcomes into numerous downstream tasks. In the principal task of cross-modal image-text retrieval, we employ CLIP with ViT-B/32 as the baseline and target model by default. All experiments are conducted on a single RTX 3090 GPU using the AdamW optimizer. During both training phases, the model is trained for five epochs with a batch size of 256 and 500 warmup steps.

For the image classification task on the WebFG dataset, we align with the field's prevalent models for a fair comparison by employing the ResNet-50 model enhanced by CLIP for feature extraction and the CLIP image encoder as our estimator. Training and testing are executed on single RTX 3090 GPU, with an input image resolution of 448×448. The batch size and initial learning rate are specified as 64 and 1e-5, respectively. In the first phase, the estimator is trained with data modeled by a Gaussian Mixture Model (GMM), which considers the classification and matching losses of all training samples, with the GMM probability threshold of 0.95. The classification task leverages the CLIP protocol, where a fixed prompt ("This is a picture of") is prepended to category texts.

For the image retrieval task, we use CLIP ViT-B/32 as the baseline, with a batch size set to 128, an initial learning rate of 5e-6, and the number of epochs set to 10. Following the setup of the PRISM [5], we set the parameter for sampling positive examples by the random sampler of the dataloader to 4, and adjust the number of positive examples sampled per epoch to one-fourth of the original parameter according to the increase in batch size. In this task, we also adopt a two-stage training approach. The strictly clean in-domain training data for the first stage is obtained using a GMM model with a probability setting of 0.8.

B Related work

B.1 Noise Mitigation in Cross-Modal Matching

The cross-modal matching task [24–28] serves as a fundamental component in multimodal learning. However, the inherent difference in information density between these modalities leads to high annotation costs and inconsistent annotation quality, rendering cross-modal tasks particularly vulnerable to label noise. Some approaches explicitly identify and correct noisy samples through cross-prediction between concurrently trained dual models [1, 7, 29], while others [2, 9] implicitly estimate the probability of sample noise, reducing its training impact by adjusting the loss function.

NCR [1] employs the memorization capacity of its counterpart model for simple clean samples to rectify the output results. BiCro [7] utilizes the consistency of similarity score distributions from a Siamese model ensemble on noisy data, alongside anchors modeled on the loss distribution via a Beta-Mixture-Model (BMM), to filter out noisy samples. NPC [2], deviating from the dual-model training schemes, introduces a two-stage single-model training approach that reduces training overhead by replacing two backward passes with one forward and one backward pass. Specifically, the first stage estimates the impact of potentially noisy samples on model performance by constructing a high-quality clean sample bank; the second stage then utilizes these estimates to reweight the loss function. However, current methods for distinguishing clean from noisy samples rely on numerous hyperparameters that are closely linked to dataset size and model capacity. This dependency not only limits their adaptability to various downstream tasks but also makes them challenging to deploy in real-world applications.

B.2   Noise Mitigation in Image Classification

Image classification is vulnerable to training data noise, due to varied noise types and strong model memorization. Noise in datasets manifests in two primary forms: synthetic alterations and those arising from real-world scenarios. The former typically involves shuffling the labels of a subset of the data or retaining the labels while introducing corresponding category images from external datasets. The latter entails substituting images for a random selection of data points with those sourced from image search engines. Existing approaches are categorized based on their operational focus: loss correction [30–40] and sample selection [41–43, 10, 44]. Loss correction methods typically incorporate a regularization term into the loss function, implicitly reweighting clean and noisy samples within the loss. Sample selection strategies, in contrast, explicitly differentiate between clean and noisy samples, applying distinct processing to each category during loss computation. Representative for the loss correction category, [31] aims to generalize ordinary Cross-Entropy loss and MAE loss by setting the loss threshold to iid and ood noisy samples. DivideMix [10] concurrently trains two networks, each utilizing the data partitioning from the other network to distinguish between clean and noisy samples based on loss values, thereby mitigating the influence of confirmation bias inherent within each network. PNP [41] framework employs a unified predictive network to estimate the in-distribution (iid), out-of-distribution (ood), and clean probabilities for a given sample. Co-training trained on a sample that has a lower loss, and with the different predictions by its siamese network.

B.3   Noise Mitigation in Image Retrieval.

Although image retrieval tasks focus on pairwise relationships, the noise predominantly originates from image categorization errors. Analogous to image classification tasks, this can be bifurcated into in-domain [45] and open-set noise [5]. In terms of task configuration, noise retrieval typically operates at the category level, treating images within the same category as positive instances. PRISM [5] tries to find noisy image samples by finding the outliers score in the whole similarity matrix from the same category. The generalization ability of the image feature is ensured by a broader query bank restored multi-view of it. TITAN [46] utilizes prototypes to be representative of the anchor of the clean and noisy samples and then generates synthetic samples by a combination of prototypes for substitution of noisy samples. T-SINT [47] utilizes more negative samples by the interaction between noisy samples and negative samples that belong to another category.

C   Proofs

C.1   Proof of High-dimensional Orthogonality

Suppose $u, v \in \mathbb{R}^d$ are any two random vectors. The cosine similarity $\cos(u, v) \sim \mathcal{N}(0, d^{-1})$. The probability that $\cos(u, v)$ is within a specific range $[-a, a]$ is denoted as:

$$P(-a \leq \cos(u, v) \leq a) = \Phi\left(\frac{a}{\varsigma}\right) - \Phi\left(\frac{-a}{\varsigma}\right), \tag{7}$$

where Φ represents the CDF of the standard normal distribution, and $\varsigma = \frac{1}{\sqrt{d}}$ is the standard deviation of the cosine similarity. When $d = 1024$ and $a = 0.1$, there are

$$\varsigma = \frac{1}{\sqrt{1024}} = \frac{1}{32}, \tag{8}$$

and

$$P(-0.1 \leq \cos(u,v) \leq 0.1) = \Phi\left(\frac{0.1}{1/32}\right) - \Phi\left(\frac{-0.1}{1/32}\right) \approx 0.9986. \tag{9}$$

C.2 Proof of Theorem 1

In the Section. 2.2, we propose that Theorem 1 about the relative relationship of pairs in the original entire space, will not change after transmitting to the narrow cone space of the trained model, and there is always a boundary r concentrated on most random vectors.

To prove this Theorem, we first introduce a useful lemma of monotonicity of cosine similarity proposed by [14], indicating that the cosine similarity between two vectors increases with a high probability after one feedforward computation consisting of a linear transformation and ReLU computation.

Lemma 1. *Suppose $u, v \in \mathbb{R}^{d_{in}}$ are any two fixed vectors such that $\|u\| = r \|v\|$ for some $r > 0$, $\mathbf{W} \in \mathbb{R}^{d_{out} \times d_{in}}$ is a random weight matrix where each element $\mathbf{W}_{k,l} \sim \mathcal{N}(0, d_{out}^{-1})$ for $k \in [d_{out}]$, $l \in [d_{in}]$, and $\mathbf{b} \in \mathbb{R}^{d_{out}}$ is a random bias vector such that $\mathbf{b}_k \sim \mathcal{N}(0, d_{out}^{-1})$ for $k \in [d_{out}]$. If $\cos(u,v) < (\frac{1}{2}(r + \frac{1}{r}))^{-1}$, then the following holds with probability at least $1 - O(1/d_{out})$.*

$$\cos(\sigma(\mathbf{W}u + \mathbf{b}), \sigma(\mathbf{W}v + \mathbf{b})) > \cos(u,v). \tag{10}$$

Proof of Theorem. 1. Let $\mathbb{R}^{d_{in}}$ be the original space before being transmitted in a neural network. Suppose $u, v \in \mathbb{R}^{d_{in}}$ are any two random vectors with $\cos(u,v) \approx 0$. $u_c, v_c \in \mathbb{R}^{d_{in}}$ is a pair of clean vectors with $\cos(u_c, v_c) > 0$, while $u_n, v_n \in \mathbb{R}^{d_{in}}$ is a noisy pair with $\cos(u_n, v_n) < 0$. Given a Neural Network $F(x) = f_t(f_{t-1}(\ldots f_2(f_1(x)))) \in \mathbb{R}^{d_{out}}$ with t layers. $f_i(x) = \sigma_i(\mathbf{W}_i x + \mathbf{b}_i)$ denotes i^{th} layer, where $\sigma(\cdot)$ indicates activation function. $\mathbf{W}_i \in \mathbb{R}^{d_{out}^i \times d_{in}^i}$ is a random weight matrix where each element $\mathbf{W}_i^{k,l} \sim \mathcal{N}(0, 1/d_{out}^i)$ for $k \in [d_{out}^i]$, $l \in [d_{in}^i]$, and $\mathbf{b}_i \in \mathbb{R}^{d_{out}^i}$ is a random bias vector such that $\mathbf{b}_i^k \sim \mathcal{N}(0, 1/d_{out}^i)$ for $k \in [d_{out}^i]$. We would like to prove that there are always be a boundary β, satisfying:

$$\cos(F(u_n), F(v_n)) < \cos(F(u), F(v)) \approx \beta < \cos(F(u_c), F(v_c)), \tag{11}$$

which is equivalent to proving.

$$\cos(f_i(u_n), f_i(v_n)) < \cos(f_i(u), f_i(v)) \approx \beta_i < \cos(f_i(u_c), f_i(v_c)), \tag{12}$$

where β_i is the boundary of ith layer.

We first consider the cosine similarity between u and v as:

$$\cos(u,v) = \frac{u \cdot v}{\|u\| \|v\|}. \tag{13}$$

After a linear transformation of ith layer, the cosine similarity of $\cos(\mathbf{W}_i u + \mathbf{b}_i, \mathbf{W}_i v + \mathbf{b}_i)$ denotes:

$$\cos(\mathbf{W}_i u + \mathbf{b}_i, \mathbf{W}_i v + \mathbf{b}_i) = \frac{(\mathbf{W}_i u + \mathbf{b}_i) \cdot (\mathbf{W}_i v + \mathbf{b}_i)}{\|\mathbf{W}_i u + \mathbf{b}_i\| \|\mathbf{W}_i v + \mathbf{b}_i\|}. \tag{14}$$

Since $\mathbf{b}_i$ has a mean of zero and is independent from $\mathbf{W}_i u$ and $\mathbf{W}_i v$, the expectation of $\mathbf{b}_i$ and $(\mathbf{W}_i u + \mathbf{b}_i) \cdot \mathbf{W}_i v + \mathbf{b}_i)$ can be signified as:

$$\mathbb{E}[\mathbf{b}_i] = 0, \tag{15}$$

$$\mathbb{E}[(\mathbf{W}_i u + \mathbf{b}_i) \cdot (\mathbf{W}_i v + \mathbf{b}_i)] = \mathbb{E}[(\mathbf{W}_i u \cdot \mathbf{W}_i v)] = \sum_{i=1}^{n} \sum_{i=1}^{n} \frac{1}{d_{out}^i} u_k v_k = \frac{1}{d_{out}^i}(u \cdot v). \tag{16}$$

Additionally, we have

$$\|\mathbf{W}_i u + \mathbf{b}_i\|^2 = \mathbf{W}_i u \cdot \mathbf{W}_i u + 2\mathbf{W}_i u \cdot \mathbf{b}_i + \mathbf{b}_i \cdot \mathbf{b}_i. \tag{17}$$

Due to $\mathbb{b}^k \sim \mathcal{N}(0, 1/d_{out}^i)$, as d_{o}^iut increases, the term of $2\mathbf{W}_i u \cdot \mathbf{b}_i$ and $\mathbf{b}_i \cdot \mathbf{b}_i$ become negligible, which implies

$$\|\mathbf{W}_i u + \mathbf{b}_i\|^2 \approx \mathbf{W}_i u \cdot \mathbf{W}_i u = \sum_{i=1}^{n} (\mathbf{W}_i u)^2. \tag{18}$$

Therefore, the expectation of $\|\mathbf{W}_i u + \mathbf{b}_i\|^2$ is approximate to

$$\mathbb{E}\left[\|\mathbf{W}_i u\|^2\right] = \sum_{k=1}^{n} u_k^2 \frac{1}{d_{out}^i} = \frac{\|u\|}{d_{out}^i}, \tag{19}$$

and

$$\begin{aligned}
\cos(\mathbf{W}_i u + \mathbf{b}_i, \mathbf{W}_i v + \mathbf{b}_i) &\approx \frac{\mathbb{E}[\mathbf{W}_i u \cdot \mathbf{W}_i v]}{\sqrt{\mathbb{E}[\|\mathbf{W}_i u + \mathbf{b}_i\|^2]\mathbb{E}[\|\mathbf{W}_i v + \mathbf{b}_i\|^2]}} \\
&= \frac{\frac{1}{d_{out}^i}(u \cdot v)}{\sqrt{\frac{1}{d_{out}^i}\|u\|^2 \cdot \frac{1}{d_{out}^i}\|v\|^2}} \\
&= \cos(u, v).
\end{aligned} \tag{20}$$

Based on Eq. 20, with $\cos(u_n, v_n) < \cos(u, v) \approx 0 < \cos(u_c, v_c)$, there are

$$\cos(\mathbf{W}_i u_n + \mathbf{b}_i, \mathbf{W}_i v_n \mathbf{b}_i) < \cos(\mathbf{W}_i u + \mathbf{b}_i, \mathbf{W}_i v + \mathbf{b}_i) < \cos(\mathbf{W}_i u_c + \mathbf{b}_i, \mathbf{W}_i v_c + \mathbf{b}_i). \tag{21}$$

Since the activation function σ is a monotonically increasing function, it follows

$$\cos(f_i(u_n), f_i(v_n)) < \cos(f_i(u), f_i(v)) < \cos(f_i(u_c), f_i(v_c)). \tag{22}$$

Due to Lemma. 1, $\cos(f_i(u), f_i(v))$ will be increase with the transmitting layers, and $\cos(f_i(u), f_i(v))$ will always be a $\beta_i > 0$, to satisfy:

$$\cos(f_i(u_n), f_i(v_n)) < \cos(f_i(u), f_i(v)) \approx \beta_i < \cos(f_i(u_c), f_i(v_c)). \tag{23}$$

After transmitting each layer, Eq. 23 are always satisfied. When transmitting a neural network with t layers, we have

$$\cos(F(u_n), F(v_n)) < \cos(F(u), F(v)) \approx \beta < \cos(F(u_c), F(v_c)). \tag{24}$$

$\square$

(a) parameters   (b) 128-th dim of image   (c) 256-th dim of image   (d) 512-th dim of image

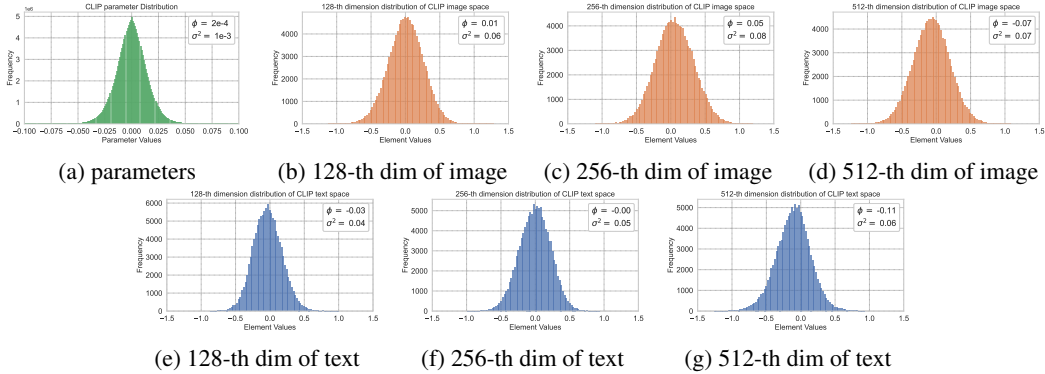(e) 128-th dim of text   (f) 256-th dim of text   (g) 512-th dim of text

Figure 3: The illustrations of several distributions on CC120K. (a) The parameter distribution. (b-d) The distribution of image features for the 128th, 256th, and 512th dimensions. (e-g) The distribution of text features for the 128th, 256th, and 512th dimensions.

C.3 Proof of Orthogonality Validity in Cone Space

Although we have demonstrated in Appendix. C.1 that in the original high-dimensional space, the cosine similarity between two randomly selected vectors—each dimension following a Gaussian distribution—typically converges near the orthogonal boundary, this property may not necessarily extend to the subspace of the shared embedding space maintained by the trained models. Specifically,

18

for real image-text pairs, the subspace may deviate from the orthogonal characteristics observed in the original space. Thus, it is essential to investigate whether the orthogonality property holds within the cone space for the image-text subdomain post-training.

To explore this, we first analyze the distribution of several dimensions of image and text features from the CC120K dataset, as illustrated in Figure. 3. The results reveal that all vector dimensions, including trained parameters, exhibit a Gaussian distribution with near-zero means. If the dimensions of the trained embedding space follow Gaussian distributions, the process of selecting random vectors within this space would be analogous to that of the original space, thereby preserving the orthogonality property. Here, we present the following theorem: The output features of large-scale models tend to Gaussian distribution. The detailed theorem and proof are provided below.

Theorem 2 (Output features tends to Gaussian). *Given a Neural Network $F(x) = \{f_t(f_{t-1}(\ldots f_2(f_1(x))))\} \in \mathbb{R}^{d_{out}}$ with t layers. $f_l(x) = \phi_l(\mathbf{W}_l x + \mathbf{b}_l)$ denotes the lth layer, where $\phi(\cdot)$ indicates the activation function, and the final layer $f_t(x) = \mathbf{W}_t x + \mathbf{b}_t$ is a fully-connected layer without an activation function for common space projection. Let $x^k \in \mathbb{R}^{d_{in}^k}$ be the sample feature that will be transmitted into the kth layer, where x^1 denotes the original feature with an unknown distribution $x^1 \sim (\mu_x, \sigma_x^2)$. $\mathbf{W}_k \in \mathbb{R}^{d_{out}^k \times d_{in}^k}$ is a random weight matrix where each element $w_{ij}^k \sim \mathcal{N}(0, \sigma_w^2)$ for $i \in [d_{out}^k]$, $j \in [d_{in}^k]$, and $\mathbf{b}_k \in \mathbb{R}^{d_{out}^k}$ is a bias vector such that $b_i^k \sim \mathcal{N}(0, \sigma_w^2)$ for $i \in [d_{out}^k]$. In such a neural network, linear layers lead features x gradually to a Gaussian distribution from any initial distribution, and as $|d_{in}|$ is sufficiently large, $F(x) \sim \mathcal{N}(0, \sigma^2)$.*

Proof of Theorem. 2. For the kth layer ($k \in [t]$), we first calculate the expectation and variance of the linear combination $\sum_{j=1}^{d_{in}^k} w_{ij}^k x_j^k$. For the expectation, since w_{ij}^k and x_j^k are independent and $\mathbf{w}_{ij}^k \sim \mathcal{N}(0, \frac{1}{d_{out}^k})$, we have:

$$\mathbb{E}\left[\sum_{j=1}^{d_{in}^k} w_{ij}^k x_j^k\right] = \sum_{j=1}^{d_{in}^k} \mathbb{E}[w_{ij}^k]\mathbb{E}[x_j^k] = \sum_{j=1}^{d_{in}^k} (0 \times \mathbb{E}[x_j^k]) = 0. \tag{25}$$

For variance, since w_{ij}^k and x_j^k are independent, we have:

$$\begin{aligned}
\text{Var}\left(\sum_{j=1}^{d_{in}^k} w_{ij}^k x_j^k\right) &= \sum_{j=1}^{d_{in}^k} \text{Var}(w_{ij}^k x_j^k) = \sum_{j=1}^{d_{in}^k} \mathbb{E}\left[(w_{ij}^k)^2 (x_j^k)^2\right] \\
&= \sum_{j=1}^{d_{in}^k} \mathbb{E}\left[(w_{ij}^k)^2\right] \mathbb{E}\left[(x_j^k)^2\right] \\
&= \sum_{j=1}^{d_{in}^k} \sigma_{w^k}^2 \left(\text{Var}(x_j^k) + (\mathbb{E}[x_j^k])^2\right) \\
&= \sum_{j=1}^{d_{in}^k} \sigma_{w^k}^2 \left(\sigma_{x^k}^2 + \mu_{x^k}^2\right) = d_{in}^k \sigma_{w^k}^2 \left(\sigma_{x^k}^2 + \mu_{x^k}^2\right).
\end{aligned} \tag{26}$$

Since w_{ij}^k are independently distributed Gaussian random variables, and x_j^k has a known mean and variance, the sum of $w_{ij}^k x_j^k$ can apply to a generalized Central Limit Theorem. We have

$$\frac{\sum_{j=1}^{d_{in}^k} w_{ij}^k x_j^k - \mathbb{E}\left[\sum_{j=1}^{d_{in}^k} w_{ij}^k x_j^k\right]}{\sqrt{\text{Var}\left(\sum_{j=1}^{d_{in}^k} w_{ij}^k x_j^k\right)}} \xrightarrow{d} \mathcal{N}(0, 1), \tag{27}$$

which is equivalent to

$$\frac{\sum_{j=1}^{d_{in}^k} w_{ij}^k x_j^k - 0}{\sqrt{d_{in}^k \sigma_{w^k}^2 (\sigma_{x^k}^2 + \mu_{x^k}^2)}} \xrightarrow{d} \mathcal{N}(0, 1). \tag{28}$$

19

Therefore,

$$\sum_{j=1}^{d_{in}^k} w_{ij}^k x_j^k \xrightarrow{d} \mathcal{N}(0, d_{in}^k \sigma_{w^k}^2 (\sigma_{x^k}^2 + \mu_{x^k}^2)). \tag{29}$$

Due to $b^k \sim \mathcal{N}(0, \sigma_b^2)$, we finally get

$$\sum_{j=1}^{d_{in}^k} w_{ij}^k x_j^k + b_i^k \xrightarrow{d} \mathcal{N}\left(0, d_{in}^k \sigma_{w^k}^2 (\sigma_{x^k}^2 + \mu_{x^k}^2) + \sigma_b^2\right). \tag{30}$$

Although activation functions truncate the Gaussian distribution after each linear layer, the samples still gradually approach a Gaussian distribution from the initial unknown distribution as they pass through the layers. Furthermore, because there is a fully connected layer (layer) without an activation function before mapping to the final common space, the final feature distribution will approximate a Gaussian distribution, as follows:

$$F(x) \sim \mathcal{N}(0, d_{in}^t \sigma_{w^t}^2 (\sigma_{x^t}^2 + \mu_{x^t}^2) + \sigma_b^2). \tag{31}$$
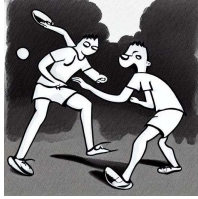
$\square$

D   SDM Visualization

We visualize some representative samples from our synthetic domain originating from COCO by using SDM. The results are shown in Figure. 4. We generate two styles of image based on the MSCOCO caption, and then use pre-trained multimodal models to calculate cosine similarity with the SDM-generated image and original caption.

Figure 4: Examples of generated SDM dataset. The first row is in sketch style, while the second row is in cartoon style.